Nanoscale

PAPER

View Article Online
View Journal | View Issue

Cite this: *Nanoscale*, 2024, **16**, 12081

Hand-crafted potent hydroxyl-rich husk succoured Fe_3O_4 @ Cu, Mn, Ni, Co – tetra-metallic heterogenous nanocomposite as a catalytic accelerant†

Ramya Ravichandran,[a] Arun Annamalai,[a] Kumaresan Annamalai,[a] Anandhavalli Jeevarathinam,[a] Suresh Ranganathan [b] and Sundaravadivel Elumalai *[a]

An innovative means of synthesizing mechanically recoverable ternary nanocomposite (NC) comprising Fe_3O_4 supported on *Oryza sativa* husk (OSH) and ornamented with 3d tetra-metals (M = Mn, Co, Ni, Cu) is proposed using a manual grinding method. This NC was prepared *via* a one-step manual method. The added advantage of this method is the non-usage of solvents during the synthesis of the NC. *In situ*, the NPs were grown on OSH-supported magnetite NPs, where they combined to form a matrix to facilitate the formation of the metal NPs in it. The as-crafted *Oryza sativa* husk-supported magnetite @ tetra-metallic nanocore hybrid (OSFTC) was confirmed *via* several characterisation techniques, such as XRD, FT-IR, HR-TEM, FE-SEM, XPS, VSM, NMR, and UV-vis analysis. The interesting twist in this NC is that the leaching-in of metals toward the core of the NC increases the magnetic nature of the composite as evidenced by VSM analysis. The electrostatic attraction between NPs formed and the matrix plausibly results in enhanced photocatalytic degradation of pharma-waste in an efficient way. The activity of the OSFTC increases for ciprofloxacin and paracetamol by 67 and 71%. Furthermore, the hydrogenation of anthropogenic pollutants *via* a foreign agent yields a good conversion percentage of 92%. In addition, the noxious hexavalent chromium is converted to a trivalent cation with the help of OSFTC, indicating good conversion under ambient conditions. Herein, OSFTC also exhibited effective activity against both Gram-positive and Gram-negative bacteria. Moreover, the ternary composite demonstrates consistent and commendable activity against pharmaceutical compounds and carcinogenic pollutants. The OSFTC was designed in a way to perform the cleavage of bonds for toxic materials efficiently.

Received 19th March 2024,
Accepted 16th May 2024

DOI: 10.1039/d4nr01211a

rsc.li/nanoscale

1. Introduction

This new era is going toward a catastrophe of energy scarcity and increased environmental degradation due to recent innovations and a growing population. A crucial issue in our day-to-day life that raises a risky alarm is the concern for water. Water is a highly significant aspect of our lives because it is not only necessary for our physical survival but also for many home and industrial tasks, such as cleaning and product creation. Owing to the water management crisis, unsustainable exploitation and unmanageable contamination are currently "hot issues". The expansion of modern society results in the proliferation of harmful substances, such as heavy metals, fluorides, dyes,[1–3] pesticides,[4,5] and pharmaceuticals, into aquatic environments, posing significant threats to both organisms and human populations. Despite this, the prevalence of bacterial infections remains a significant threat to human survival, particularly in our increasingly technologically advanced world.[6,7] The escalating rate of microbial resistance poses a grave danger by putting various species at risk. Advanced materials, such as covalent organic frameworks, metal–organic frameworks, and metal nanocomposites,[8,9] have garnered significant attention due to their diverse applications in the synthesis of nanoparticles.[10,11]

To address the challenges confronting humanity, it is imperative to create a material capable of withstanding the obstacles posed by pathogens. Nanotechnology offers a ray of hope in overcoming the threats encountered in our daily lives.[12] Among the wide variety of materials available in this

[a]*Department of Chemistry, SRM Institute of Science and Technology, Kattankulathur, Tamil Nadu – 603203, India. E-mail: sundaravadivelchem@gmail.com*
[b]*Department of Chemistry, Centre for Material Chemistry, Karpagam Academy of Higher Education, Coimbatore – 641021, India*

† Electronic supplementary information (ESI) available. See DOI: https://doi.org/10.1039/d4nr01211a

field, nanocomposites are noticed for their increased efficiency, rather than individual nanoparticles. The ultimate aim in choosing materials at the nanoscale is that they exhibit exceptional physicochemical properties compared to bulk materials, including high porosity, durability, tunable structure, increased surface area, and unique optoelectronic characteristics. In this era, the development of nanocomposites (NC) has reached its peak due to the synergistic effect of the precursors added during the preparation of the material.[13–15] These materials use different ways to eradicate waste from water. Separation methods to eliminate carcinogenic pollutants involve techniques, such as adsorption,[16] chemical coagulation, reverse osmosis,[17,18] and precipitation. However, their limitations, such as high expenses, difficult procedures, and the generation of hazardous by-products, underscore the need to explore alternative approaches for treating such organic waste. Despite this, metal leaching during the treatment process also plays a major role in imparting hazardous effects.

To resolve these difficulties faced by researchers, eco-friendly approaches to synthesizing metal nanoparticles, along with improving their magnetic properties, have garnered considerable interest for their potential application as catalysts or as the central component of nanohybrid composites.[19–21] These materials hold promise as reusable green catalysts for transforming harmful organic compounds into benign products. The presence of size-related factors, such as large surface area, enhanced reactivity, high biocompatibility, and the inclusion of a hydroxyl group on the capping agent, facilitates an efficient formation of nanoparticles.[22,23] To minimize the toxicity associated with the chemicals utilized in nanoparticle preparation, there is a growing emphasis on selecting greener stabilizing agents. In contrast to conventional chemical and physical methods, nanoparticle synthesis using waste-derived plant materials presents numerous benefits due to its simplicity, feasibility under ambient conditions, cost-effectiveness, and environmentally friendly nature. Green synthesis methods involve utilizing harmless solvents, such as water and natural extracts, to produce nanoparticles that are relatively free from pollutants. Herein, rice husk (OSH) was used as a stabilizing agent because it contains numerous amounts of hydroxyl groups. These groups play an important role in grasping the nanoparticles that are formed during the synthesis of NC. The utilization of greener agents in nanoparticle synthesis has garnered significant attention due to their non-toxic nature, accessibility, and potential for biological activity.[24,25] The OSH forms a matrix-like structure with the magnetite NPs, which plays a major role in preventing the aggregation of NPs.[26–28]

Various noble metals, including gold (Au), silver (Ag), palladium (Pd), and platinum (Pt), have been utilized in the synthesis of nanomaterials for diverse applications.[29–31] However, due to their high cost, non-biodegradability, and other constraints, we pursue an alternative metal that can complement the properties of noble metals.[32–34] In this work, we use the transition metals of the first series which are regarded as cost-effective metals, compared to noble metals.[35] By utilizing a bimetallic catalyst, instead of a monometallic one, the requirement for noble metals for the preparation of nanomaterials can be reduced. Recent advancements in heterogeneous catalysis emphasize the significant advantages of bimetallic nanoparticles stabilized by plant-mediated extracts.[36] These advantages include prolonged release times, resulting in enhanced antibacterial activity against both Gram-positive and Gram-negative bacteria. Because of its high surface area, the penetration into the bacterial cell membrane through the cell wall is facilitated, which leads to the demise of the bacterium.

A greener way of synthesizing a ternary hybrid nanocomposite was successfully designed using a simple one-step grinding method. The nanocomposite utilizes OSH as the stabilizing material and aims to improve the efficiency of photocatalytic degradation of pollutants. A material with the ability to seamlessly integrate both organic and inorganic properties for the fabrication of photocatalytic membranes was developed.[9] At the core of the nanohybrid, magnetite nanoparticles served as the magnetic component. The structure of the nanohybrid comprises both trivalent (Fe^{3+}) and divalent (Fe^{2+}) states of ions.[37,38] Half of the octahedral positions are occupied by Fe^{2+} ions, while Fe^{3+} ions bridge the lateral tetrahedral and octahedral sites, resulting in the formation of a cubic inverse spinel structure. Researchers are interested in leveraging its exceptional antiferromagnetic properties to incorporate reusability features into the nanocomposite, allowing it to perform effectively for multiple cycles.[39]

The synthesis of a ternary nanohybrid composite was effectively accomplished using a manual one-step grinding method. This study assesses the efficacy of the composite in treating carcinogenic pollutants,[40–42] pharmaceutical wastes,[43–46] anti-bacterial inhibition properties, conversion of nitro-aromatics,[47] and reduction of hazardous ions[48] in water. The ternary nanocomposite exhibits favourable activity, affordability, environmental friendliness, and excellent stability. This ternary composite uses cheap metals, such as cobalt, nickel, *etc*., Hence, this composite paves the way for cost-effective material synthesis. This method is prepared through energy-efficient ways. Consequently, we assert that the ternary nanocomposite proposed here is a promising material for addressing the significant challenges associated with water scarcity and combating water-borne pathogens that pose risks to living organisms.

2. Experimental section

2.1 Materials

Oryza sativa husks were collected in the Cuddalore district in the month of February after the completion of the harvesting process. Nickel chloride hexahydrate ($NiCl_2{\cdot}6H_2O$ – 98%), cobalt chloride hexahydrate ($CoCl_2{\cdot}6H_2O$ – 98%), manganese chloride tetrahydrate ($MnCl_2{\cdot}4H_2O$), copper chloride dihydrate ($Cucl_2{\cdot}2H_2O$ – 98%), ferric chloride hexahydrate ($FeCl_3{\cdot}6H_2O$ – 97%), ferrous chloride tetrahydrate ($FeCl_2{\cdot}4H_2O$ – 98%), hydrochloric acid (HCl – 33%), and sodium hydroxide (NaOH –

97%) were purchased from Sigma Aldrich and Merck company. Sodium borohydride ($NaBH_4$ – 95.5%), potassium dichromate ($K_2Cr_2O_7$), and 4-nitrophenol were obtained from SD Fine Chemicals Private Limited. The chemicals used in this experiment were done without any further purification. Paracetamol (PR) and ciprofloxacin (CP) were procured from a pharmaceutical company. The entire synthesis process exclusively employs Milli-Q grade water.

2.2 Preparation of magnetite nanoparticles

The co-precipitation method is employed to create magnetic nanoparticles. In this procedure, a round bottom flask containing a solution of 0.5 M hydrochloric acid (4 mL) is combined with freshly dissolved $FeCl_2{\cdot}4H_2O$ and $FeCl_3{\cdot}6H_2O$ in a 1 : 2 ratio at concentrations of 0.002 M and 0.004 M, respectively. Subsequently, the flask was subjected to magnetic stirring for a duration of 20 minutes. Following this, 50 cc of a 1.5 M NaOH solution was introduced into the mixture, and the reaction took place with continuous stirring for 30 minutes. The emergence of a black residue signified the reduction of both ferrous and ferric ions, confirming the successful formation of Fe_3O_4 nanoparticles. The residue was collected after the solution reached neutral pH by undergoing multiple washes with water.

2.2.1 Effect of pH control over Fe_3O_4 nanoparticles. The results of the experiment highlighted the importance of pH regulation in the synthesis of iron oxide. It was noted that no reaction occurred when the pH levels were below 3. Nanoparticles of α-Fe_2O_3 were successfully generated within the pH range of 3–5. Nevertheless, the research indicated the synthesis of black-coloured Fe_3O_4 product to be favoured at increasing pH values in an alkaline environment. At pH levels ranging from 6 to 7.2, a blend of α-Fe_2O_3 and Fe_3O_4 was synthesized, while in the pH range of 10 to 12, a pure Fe_3O_4 black precipitate was obtained. Therefore, the reaction pH was upheld under strongly alkaline conditions.

2.3 Preparation of the tetra-metallic nanocomposite

The fabrication of tetra-nanometallic composites occurs in two stages through a one-step grinding technique. The mechano-grinding method to synthesize nanocomposites stands out as an excellent and environmentally friendly approach that is devoid of solvents. At first, 0.1 g of the synthesized Fe_3O_4 and 200 mg of OSH were accurately weighed and ground for 20 minutes in a mortar. This process leads to the formation of the *Oryza sativa* husk-supported magnetite NPs (OSHF) matrix. Then $CuSO_4$ (0.5 M), $NiCl_2{\cdot}6H_2O$ (0.5 M), $MnCl_4{\cdot}5H_2O$ (0.5 M), $CoCl_2{\cdot}6H_2O$ (0.5 M) was separately added to the mixture and ground well for about 20 minutes. Metal salts were added individually into the OSHF, and the mixture was meticulously ground. Subsequently, 10 mg of $NaBH_4$ was incorporated into the mixture to facilitate the reduction of metal ions in the salts. The reducing agent employed in the production of NCs aims to reduce the metal ions to their elemental zero-oxidation state, promoting the generation of nanoparticles (NPs). In this method, the OSH serves to encapsulate the produced nanoparticles, preventing their aggregation. The alteration of the metal ion is evident at this stage and is indicated by a change in the colour of the powder from brown to a deeper, dark brown shade. Ultimately, the formulated NC underwent a thorough washing process with milli-pore water five times to remove impurities. Subsequently, it was dried in a hot air oven at 70 °C for approximately 3 hours to ensure the catalyst dried completely. The methodology for the preparation of the NC is illustrated in Fig. 1 and was utilized for subsequent investigations.

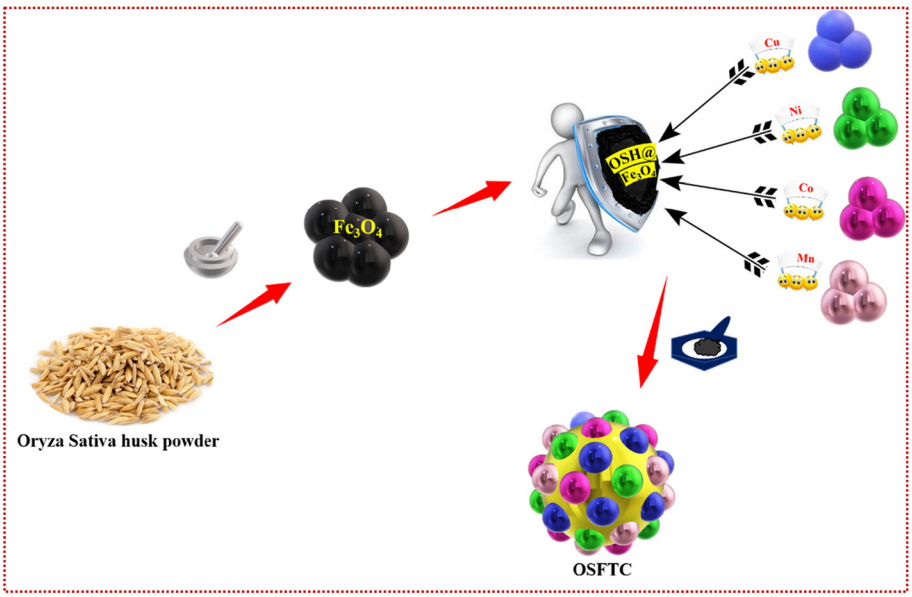

Fig. 1 Preparation scheme for the OSFTC.

2.4 Characterization of the nanocomposite

Utilizing HR-TEM, EDX, and FE-SEM analyses, the external morphology, elemental composition, and characteristics of the OSH-assisted Fe_3O_4 @ tetra nanometallic composite (OSFTC) were scrutinized. SEM imagery coupled with energy dispersive spectroscopy (EDX) data were collected and processed using the Oxford INCAX-sight software to compile all relevant information. Bruker's EDX and TEM investigations offer comprehensive insights into the size and crystallinity of a material (utilizing JEOL JEM-2100 Plus HR-TEM). The oxidation state of the metal and its chemical composition was unveiled through X-ray photoelectron spectroscopic analyses (utilizing PHI 5000 VERSA PROBE II). The functional groups assigned to the material within the 4000–400 cm^{-1} range were verified using the ALPHA-T FT-IR Spectrometer. The X-ray diffractometer was operated with Cu-Kα at a voltage of approximately 40 kV (wavelength 0.154 nm), and it scanned within Bragg's angle range 2θ (10°–80°) to precisely determine the crystalline nature of the material. Additionally, phase identification for the nanocomposite was facilitated through the GSASII software. Optical properties were investigated through UV-vis spectra in the 200–800 nm range, employing a JASCO V-670 spectrophotometer.

2.5 Photosensitive analysis

The OSFTC were employed for the photo-degradation of organic molecules, such as pharmaceutical compounds. Under ambient conditions, numerous attempts were made to optimize the choice of the concentration of toxic agents and the optimal quantity of catalyst required for the reaction. Ultimately, a stock solution comprising approximately 50 mL of 2×10^{-3} M ciprofloxacin (CP) was prepared and transferred to a beaker. Additionally, 40 mg of catalyst was introduced into another beaker, and the beakers were placed in a dark environment for careful monitoring. It was observed that the reaction did not persist in the absence of light. Subsequently, the reaction was allowed to proceed in the presence of sunlight under constant magnetic stirring. The visible reduction in colour intensity indicated the degradation of the compounds. The progress of the reaction was observed at various time points, and the corresponding data were documented using a UV-spectrophotometer with time stamps. Experiments were conducted to evaluate the efficiency of the OSFTC in degrading both antibiotics and other pharmaceuticals, showcasing the versatility of the nanocomposite as a catalyst. Usually, solutions of 50 mL containing 2×10^{-3} M of pharma-waste were prepared, and 40 mg of the catalyst was added before exposure to sunlight. The concentration of the solutions was adjusted to different strengths, and the reaction progress was observed individually under each condition. The degradation was spectroscopically analyzed with the assistance of UV-vis instrumentation.

2.6 Reduction of 4-NP and Cr^{6+} *via* the nanocomposite

To assess the catalytic efficacy of the three OSFTCs, the reduction of 4-nitrophenol (4-NPL) to 4-aminophenol (4-APL) in the presence of a reducing agent was investigated. The reaction was carried out at ambient temperature, and the conversion of the reactants was evaluated using UV-vis spectroscopy. In a beaker, 10 mL of freshly prepared 0.01 M $NaBH_4$ and 30 mL of 0.001 M 4-NPL were added. Simultaneously, varying quantities of the catalyst (10, 20, 30 mg, *etc.*) were introduced into other beakers, and the efficiency of the reaction was scrutinized. The UV-vis spectrum illustrated that increasing the amount of catalyst accelerated the conversion of the reactant. Spectra for the reaction were captured at consistent time intervals until the reaction reached completion; the initial time was recorded as "t_0". As time progressed, there was a noticeable decrease in the intensity of the yellow colour, indicating the formation of 4-APL. Similarly, the toxic Cr^{6+} agent underwent reduction to Cr^{3+} under the same ambient conditions as employed in the previous procedure for the reaction of 4-NPL. After the completion of the reaction, the catalyst was collected separately using an external magnetic field, followed by multiple washings with distilled water. The recovered composite was then used up for a reusability test for several cycles.

2.7 Anti-bacterial strain for the nanocomposite

The antibacterial inhibition was assessed using the colony-forming unit (CFU) method. Through CFU enumeration, we determined the count of viable bacteria remaining after the incubation process. To create an environment conducive to the growth of microorganisms, a sample was diluted and spread onto an agar plate containing nutrient supplements in a Petri dish. Subsequently, the Petri dish was placed in an incubator under controlled conditions, including the temperature and humidity, necessary for the survival and growth of bacterial cultures. As time progressed, the organisms proliferated and spread throughout the colonies. The CFU counting calculation is based on the formula provided below.

$$\text{CFU count} = \frac{\text{no. of colonies}}{\text{volume of culture plated (mL)}} \times \text{total dilution factor}$$

The colonies thus formed were subjected to treatment with the OSFTC synthesized in this study. To evaluate the antibacterial efficiency against both Gram-positive and Gram-negative bacteria, such as *E. coli* and *P. aeruginosa*, the synthesized NCs underwent sterilization using UV light before being employed to assess their antibacterial properties against the aforementioned bacteria. The outcomes were contrasted with the control that had streptomycin as the control agent. Streptomycin exerted its influence by inhibiting protein production carried out by the ribosomes, thereby impeding the rate of bacterial growth. In a 96-well plate set up with an initial bacterial count of 10^5, diverse drug concentrations were prepared through serial dilution using an LB medium. In summary, the experimental procedure involved subjecting bacterial cultures to different drug concentrations in a 96-well plate, incubating them with specific compounds, exposing them to LED irradiation, and monitoring the bacterial growth

survival by measuring the optical density of the treatments. The objective was to determine the minimum inhibitory concentration (MIC) and minimum bactericidal concentration (MBC) values for the drugs under different conditions. Resazurin assays were employed to assess MBC values, where MBC represents the lowest concentrations of the test substances at which the colour of resazurin remains blue. Resazurin undergoes a colour change from blue to pink in the presence of living bacteria.

3. Results and discussion

3.1 Optical capture of the OSFTC

The optical properties were studied *via* the UV-vis analysis of OSFTC, as shown in Fig. S1A.† The range of optical absorbance and the related band gaps of the synthesized OSFTC were determined by analysing the photon-absorption behaviour. The absorption curve for the pure Fe_3O_4 had a hump at 350 nm (Fig. S1A, b†); additional humps positioned at 325 nm, 370 nm, 460 nm, and 610 nm, as shown in Fig. S1A, c,† corresponding to the surface plasmon resonance peak for nickel, manganese, cobalt, and copper nanoparticles present on the OSFTC. This spectrum preliminarily confirms the formation of the OSFTC. In the presence of metal NPs, the as-crafted OSFTC undergoes a bathochromic shift, which indicates the interaction at the interface of metal NPs and the matrix. The electronic states become distinct with respect to the atoms and molecules; this modulation indicates whether the transition is allowed or not. Ultimately, the red shift enhances the optical properties of the material. The metal NPs on the OSFTC exhibit efficient electron beam deflection, enhancing the light-harvesting and light-absorbing abilities during the photocatalytic reaction. Furthermore, the band gap value was determined using the Kubela–Munk equation, which offered precise insight into the band gap of the as-synthesized material.

$$\alpha h\vartheta = k(h\vartheta - E_g)^{n/2}$$

In this context, α represents the absorption coefficient; n indicates the nature of the electronic transition; E_g stands for the optical band gap energy; ϑ represents the frequency of light; and k is the constant of proportionality. When n = 1/2, it signifies a direct-type transition, whereas n = 2 indicates an indirect transition. In this study, the band gap analysis indicates that the transition is direct. The Tauc plot was constructed using a reference *vs.* $(\alpha h\vartheta)^2$ function. When a metal was present in the material, significant energy absorption was observed at 2.2 eV for the OSFTC (Fig. S1B†). The peaks observed at 282 nm and 351 nm were attributed to the n → π* electronic transition, which occurs because of the presence of a lone pair of electrons on the hydroxyl groups in the OSH. These NPs on the surface of the matrix significantly enhance the absorption of visible light radiation by facilitating the separation of the electron–hole pairs. Increasing the quantity of metal in the composite results in an enhanced role of metal NPs within the NC, impeding the recombination of photogenerated exciton pairs. However, excessive augmentation of metal content can diminish the photo-absorption capabilities of the NC by reducing the number of available vacant sites on its surface.

3.2 Structural observations for the OSFTC

3.2.1 Spotting of crystal phase and phase purity by PXRD.

Fig. 2 illustrates the phase crystallinity, crystalline structure, and plane assembly of the NCs. The XRD analysis provided clear confirmation of the structural parameters for OSFTC NC. The plot of diffraction angle against intensity displays distinct, sharp absorption peaks that are characteristic of the responsive nature of the atoms or molecules within the material. Indexing entails an identification of the unit cell dimensions based on the positions of peaks, which serves as the initial stage of analysing a diffraction pattern. The prominent peak observed at 22.64°, 74° corresponds to the (220) plane, as depicted in Fig. 2a, which is attributed to the OSH as it acts as a capping agent for OSFTC. In Fig. S2,† the magnetite nanoparticles exhibit intense peaks at 2θ values of 30.57°, 35.91°, 43.58°, 53.82°, 57.46°, and 63.07°, which corresponds to the planes (220), (311), (400), (422), (511), and (440). The diffraction pattern obtained for the d5 supplement inverse spinel compound closely matches the JCPDS number 65-3107 (Fig. S2†). The increase in peaks corresponding to the (111), (200), and (220) planes closely match those in the JCPDS 04-0836 database, indicating a strong similarity to the face-centered cubic structure typical of copper nanoparticles (Fig. 2c). The peaks centered at 26.31°, 32.87°, 35.41°, 43.03°, 53.61°, and 62.83° are attributed to the planes, (111), (220), (311), (422), (511), and (440), confirming the presence of manganese NPs on the composite. In addition to this, the increase in peaks at 42.99°, 49.33°, and 74.06° aligns with the planes,

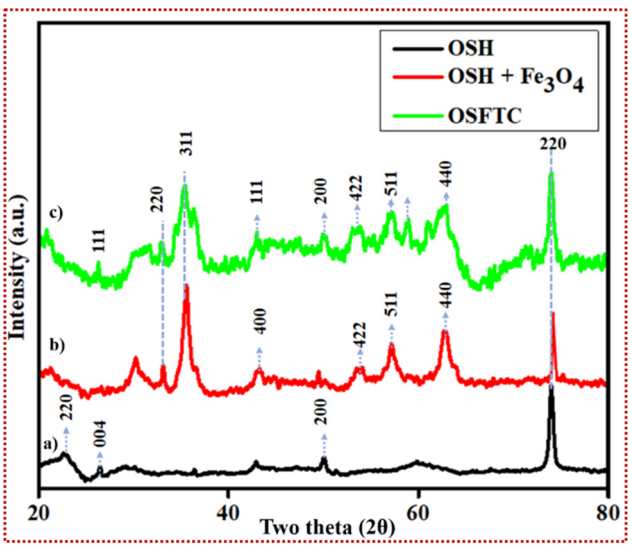

Fig. 2 XRD analysis. (a) XRD spectra for OSH, (b) XRD pattern for the OSH-supported magnetite NPs, and (c) XRD spectra of the OSFTC.

(111), (200), and (220) (Fig. 2c) that correspond to the presence of nickel nanoparticles on the material and matches the JCPDS no. 04085. In addition, it corresponds exactly to the presence of cobalt nanoparticles (JCPDS no. 89-7093). Overall, the planes exhibit similarities between the four nanoparticles due to the assignment of very similar lattice parameters of the NPs. The lattice parameter for copper is 0.37 nm; manganese is 0.281 nm; cobalt is 0.272 nm, and nickel is 0.352 nm. These values are very similar, and hence, the planes may overlap with one another. The average particle size of the nanoparticles was determined by analyzing the full width at half maximum (FWHM) of the prominent 2θ value, employing the Scherrer Equation.

$$D = k\lambda/\beta \cos\theta \quad (1)$$

The average size of the crystalline domains that lie perpendicular to the reflecting planes is denoted by D and was determined using the Scherrer Equation, where k represents the Sherrer constant; β stands for the full width at half maximum (FWHM), and λ denotes the diffraction angle. The resulting average crystalline particle size of the NC was approximately 19 nm, which matched with the HR-TEM images too. In reference to existing studies, we conducted a comparison of the X-ray diffraction (XRD) pattern of the freshly synthesized material. This comparison confirmed that the NC exhibits a phase that closely aligns with the selected area electron diffraction (SAED) pattern observed in the transmission electron microscopy (TEM) image. The exact correspondence between the Miller indices of the planes and the reflecting rings in the spot index indicated that the unit cells matched exactly for this material.

3.2.2 3D-view for the nanocomposite. The scanning electron microscope (SEM) provided a clear 3D visualization of the morphology and elemental composition of the native nanocomposite. The magnetite nanoparticles appeared spherical in shape based on the SEM image (Fig. S3a†). Subsequently, the NC image was subjected to a more detailed examination to obtain an accurate and precise resolution. The synthesized magnetite nanoparticles were spherical. The presence of the Fe_3O_4 component in the NC facilitated the separation process. The morphology of the OSH (Fig. 3f) resembles an assembly of spherical structures that combine with the magnetite NPs to form a matrix, allowing the incorporation of NPs, such as copper, cobalt, manganese, and nickel, during the NC prepa-

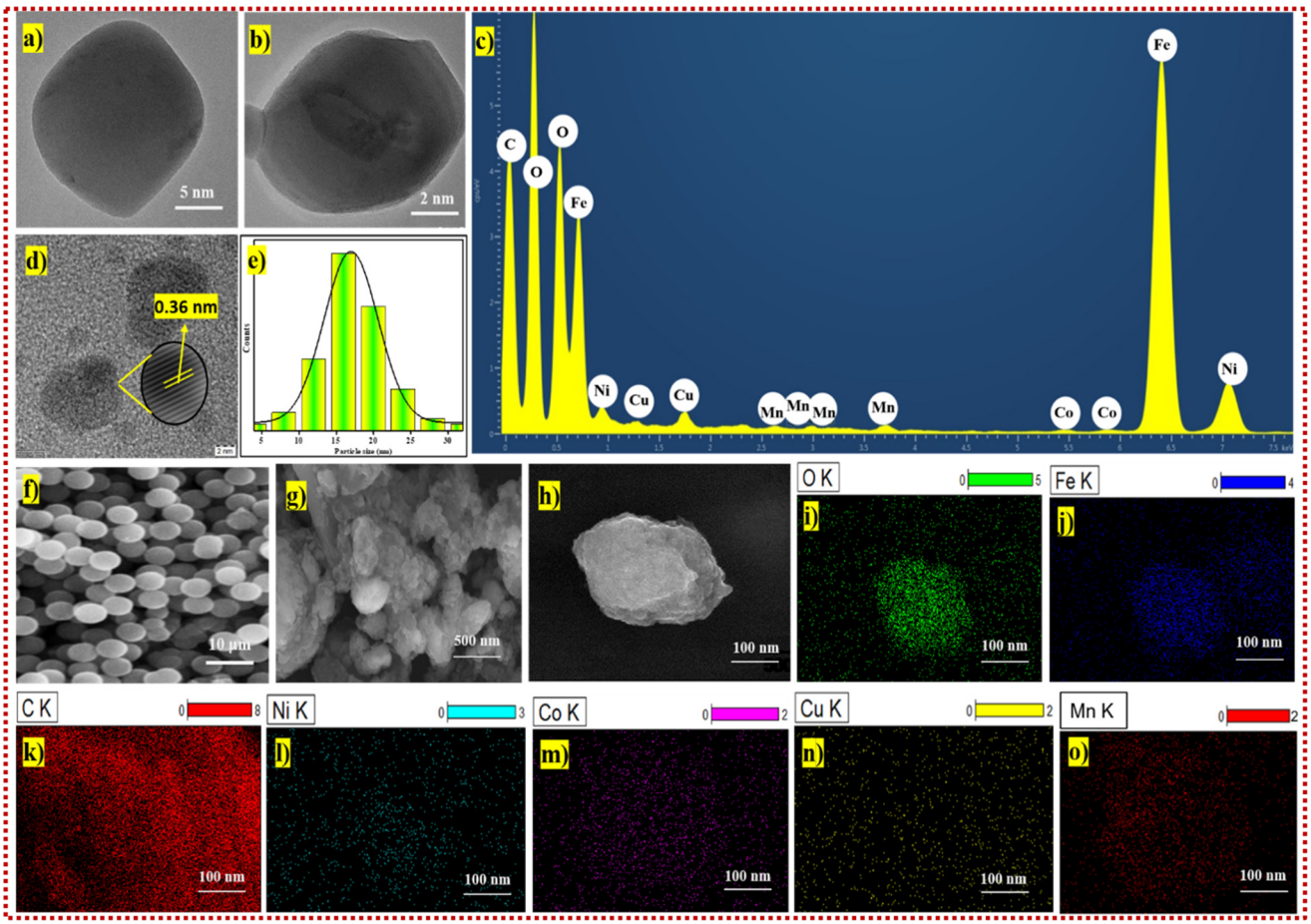

Fig. 3 Structural analysis. (a and b) TEM images of OSFTC, (c) EDX spectra for the OSFTC, (d) *d*-spacing for the OSFTC, (e) particle-size distribution of the OSFTC, (f) SEM image of the OSH, (g and h) SEM image of the OSFTC, and (i–o) elemental mapping of the OSFTC.

ration process. The three-dimensional visualization of the OSFTC is illustrated in Fig. 3(g & h), along with the elemental colour mapping for the NC in Fig. 3(i–o). The mapping images provide clear evidence for the even distribution of NPs throughout the composite, indicating no loss of metals. Upon careful examination of the highly magnified image, it was observed that the NCs exhibit a spherical shape. Elemental mapping of the NCs provides additional confirmation. In Fig. S3b,† it was observed that the NCs aggregate after undergoing four cycles of the reaction due to the adsorption of impurities. The EDX for the OSFTC were taken, confirming the presence of all four metals in the NC (Fig. S3c†). This was also further confirmed *via* the EDX analysis (Fig. S8†).

3.2.3 2D view for the nanocomposite. The transmission electron microscope (TEM) was used to greatly magnify the 2D view of the NC, allowing a detailed examination of size, morphology, and characteristics in the original state. The findings clearly show that the NC exhibited a spherical shape with uniform distribution across the coating surface (Fig. 3a–b). On average, the size of the NPs was determined to be 16 ± 2 nm using the ImageJ software (Fig. 3e). The atomic arrangement varies, depending on various parameters of the initial materials used to craft the NC. Notably, the confirmation of the NC structure aligns well with the planes observed in the XRD analysis. The alignment of the planes within the composite precisely corresponds to the pattern observed in the SAED analysis, where distinct diffraction spots resembled an organized array of rings. This observation confirms the crystalline nature of the NC that could be indexed to the face-centered cubic unit cell structure. This correlation with the planes identified in the XRD spectrum is depicted in Fig. S4b.† The spot-rings observed are generated due to the scattering of light across the material. The SAED pattern effectively establishes the presence of specific planes in the NC, confirming the existence of zero-valent NPs within it. The measured lattice spacing value, obtained by measuring the distance between two parallel fringes, was consistently determined to be 0.36 nm for all three instances (Fig. 3d). During the initiation of the reaction, the NPs within the composite played a significant role in delaying the recombination of the electron–hole pairs. This delay holds promise for enhancing the photocatalytic performance of the reaction by facilitating the channelling of electrons. The EDX spectrum image (Fig. S3c†) provides clear evidence for the presence of metals within the composite, indicating the presence of Fe, C, O, Co, Mn, Ni and Cu elements in the OSFTC. During the preparation of the NC, only a minimal amount of metal NPs was utilized, as confirmed by the weight percentage of the composite from TEM analysis (Fig. S8†).

3.3 Surface analysis of the OSFTC

3.3.1 XPS (elemental confirmation analysis). The surface analysis of the NC, including the elemental composition and various oxidation states, was conducted using X-ray photoelectron spectroscopy (XPS). This analysis reaffirmed the presence of multiple elements, such as carbon, oxygen, iron, manganese, cobalt, nickel and copper, as evidenced by the survey spectrum of the material (Fig. 4a). High-resolution spectra from XPS provide detailed insights into the binding energy of specific elements across a wide range. By analysing the binding energy requirements, we can confirm the presence of elements within the NC. Specifically, the composite OSFTC exhibits exceptional activity under ambient conditions for various reactions. The superior activity of the NC is evidenced by its increased efficiency compared to the control as confirmed through the assessment of both reaction and degradation rates. The XPS spectrum was fitted using a Gaussian–Lorentzian curve-fitting method to obtain accurate results. Using the Shirley algorithm, the background spectrum was removed from the deconvoluted spectrum of peak fittings for all the elements present in the spectrum. The spectrum of carbon (C 1s) exhibits a peak at 284.96 eV, which originates from the OSH powder; its deconvoluted spectrum appears at 284.66 eV, 285.73 eV, and 287.16 eV (Fig. 4b), which significantly contributes to the separation of electron–hole pairs during reactions under visible light. The peak is around 532.26 eV and 530.06 eV, indicating the presence of oxygen–iron (Fe–O) bonds (O 1s) that are attributed to the magnetite core of the NC (Fig. 4c). This core, composed of both iron and oxygen, is confirmed by the peaks observed in the deconvoluted spectrum at 709.54 eV and 723.34 eV, corresponding to Fe $2p_{3/2}$ and Fe $2p_{1/2}$, respectively (Fig. 4d). Additionally, the presence of manganese was evidenced by peaks at around 641.48 eV, 646.18 eV, and 653.23 eV in the deconvoluted spectrum of the NC (Fig. 4h). Moreover, peaks corresponding to copper NPs were identified at 934.9 eV, 943.7 eV, and 954.85 eV in the deconvoluted spectrum of Cu 2p (Fig. 4f).[49] The deconvoluted spectrum of copper validates the successful incorporation of zero-valent metal into the composite. The presence of nickel is validated *via* peaks at 856.29 eV, 862.34 eV, 873.94 eV, and 879.89 eV, in the deconvoluted spectrum. Whose zoomed-in image is shown in (Fig. 4g). The presence of cobalt NPs on the OSFTC was further analysed *via* the deconvoluted spectrum, which has humps at 786.07 eV, 789.53 eV, 808.88 eV, and 806.63 eV (Fig. 4e). This integration is facilitated by the presence of hydroxyl groups, where the oxygen-containing lone pairs of electrons effectively anchor the NPs formed onto the composite.

3.3.2 Picking up the functional groups. The NC was composed of functional groups that were analyzed using FT-IR analysis (Fig. 4i). This method was employed to interpret the types of functional groups bonded to the composite through infrared spectroscopy. The presence of peaks at 3471–3298 cm^{-1} indicates the existence of oxygen bonding (–O–Fe) within the Fe_3O_4 nanoparticles. Additionally, a distinct band was observed at 636 cm^{-1} that corresponded to the Fe–O–Fe bond in the Fe_3O_4 nanoparticles (Fig. 4i, (B)). The broad peak shown in (Fig. 4i, (A)) indicates the presence of hydroxyl group in the OSH. The peak at 2922 cm^{-1} became less intense, indicating the presence of aliphatic C–H in the OSH and also its retention in the composite. In addition, the peak at 1639 cm^{-1} increased due to the presence of the C═O group in the OSH powder. The peak at 1014 cm^{-1} indicates the C–H deformation, *i.e.*, the

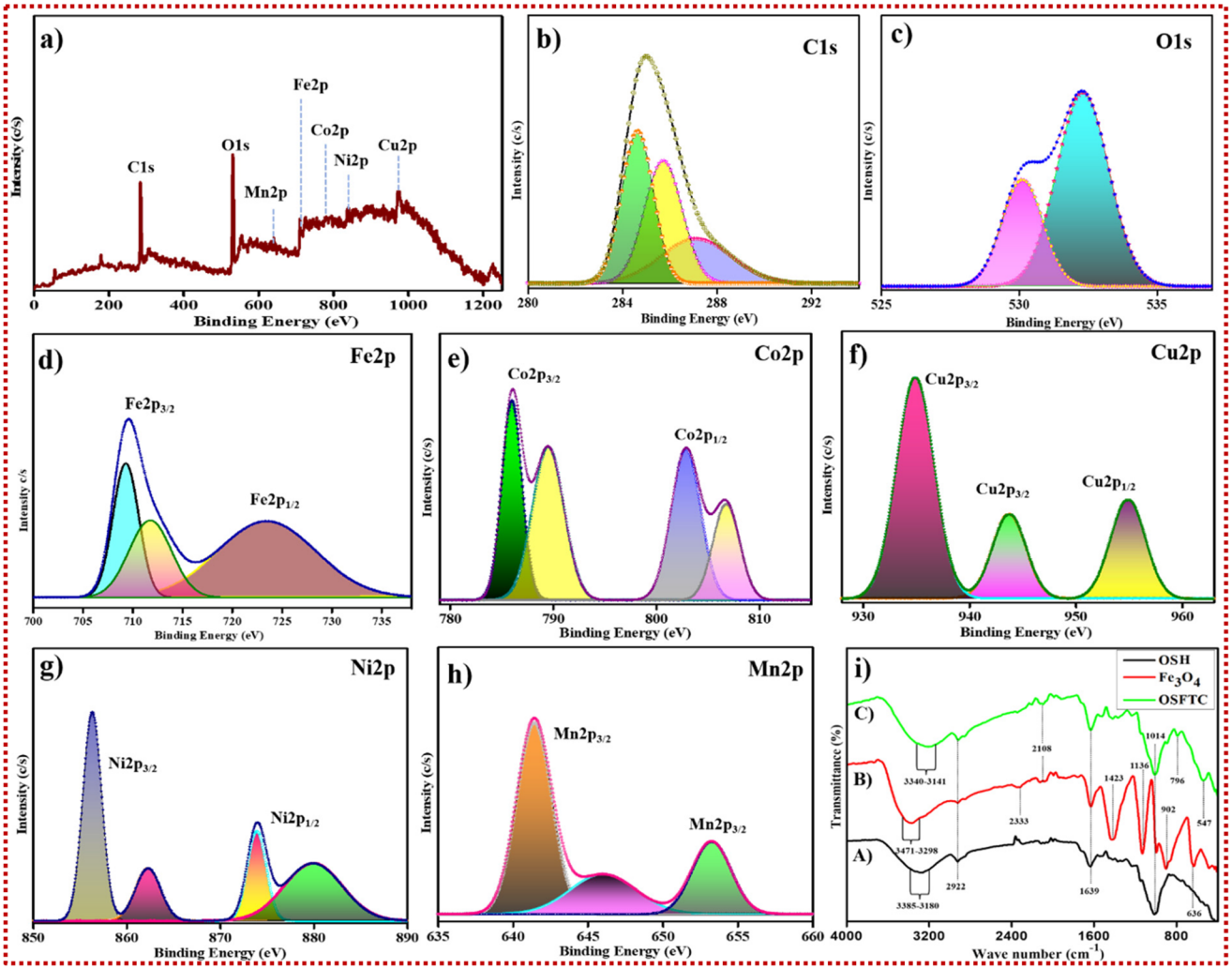

Fig. 4 Surface analysis. (a) XPS survey spectra of the OSFTC, (b–h) deconvoluted spectra of the C 1s, O 1s, Fe 2p, Co 2p, Cu 2p, Ni 2p, and Mn 2p, respectively, and (i) FT-IR spectra of the material.

presence of saturated CH_3 and CH_2 groups. A peak shift was observed in Fig. 4i, (C). from 636 cm^{-1} to 547 cm^{-1} due to the formation of the OSFTC (Fig. 4i, (C)). The presence of the hydroxyl group on the OSFTC was evidenced by the deformation and lowering of peaks from 3340 cm^{-1} to 3141 cm^{-1}. The peak that lowered to 796 cm^{-1} spikes the presence of the bending of alkene (=C–H). From all the observed analyses, the composite formed contains the magnetite NPs and the OSH powder functional groups.

3.4 Analysing the magnetic nature of the OSFTC

The magnetic properties of the nanohybrid were evaluated using a vibrating sample magnetometer (VSM) at room temperature. The strong magnetic performance of magnetite particles was confirmed by the absence of coercivity. Fig. S5b† shows the hysteresis loop of the OSFTC to demonstrate that the addition of the NPs modifies rather than eliminates the NC's magnetic behaviour. The magnetic saturation values for bare Fe_3O_4 NPs were determined to be 55.31 emu g^{-1} (Fig. S5a†) and 67.32 emu g^{-1} for the as-synthesized material. Even after the incorporation of all four metals into the matrix, we confirmed that the as-groomed NCs featured elevated magnetisation of the material as compared to the bare material. Usually, the magnetic-retention occurs by the addition of the dopant to the NC. But here, the rise in the magnetisation tells us that the metals present in the NC were paramagnetic, which causes the leaching-in of metals toward the magnetic core of the nanohybrid composite. This is the major reason for the enhancement in the magnetic behaviour of the OSFTC. Even after three cycles, the magnetisation of the composite was retained in the absence of coercivity. The bigger advantage of the NCs is their easy recoverability after the completion of the reaction without any leaching-out of metals. Hence, the catalyst remains reusable for many cycles.

3.5 Photo-catalytic eradication of noxious pollutants

Herein, a well-known pharma compound namely CP and PR was considered as pharma-waste. A known concentration of 4

$\times 10^{-3}$ M was fixed as the stock solution. Fifty millilitres of the solution were taken in separate beakers and 40 mg of the catalyst (*i.e.*, OSFTC) was added individually to each solution, and the resulting mixture was placed on a magnetic stirrer in darkness for a duration of 3 h. After 3 h, the mixture was analysed with the aid of a UV-vis spectrometer. From the spectrum obtained, we analysed that the reaction had not proceeded and there was no decrease in the intensity of the spectrum. The reaction mixture was exposed to sunlight, and samples were collected at regular intervals, typically every 15 minutes. The UV-vis spectrophotometer was utilized to assess the photodegradation efficiency of the harmful pollutants. A reduction in the intensity of the UV spectrum distinctly indicates the degradation of pollutants within the wastewater. As time progresses, the intensity of the peak diminishes. The reaction was completed in 120 minutes for CP and 150 minutes for PR (Fig. 5(a & e)). The starting time of the reaction is denoted as t_0, while the samples collected at regular time intervals are labelled as t. The degradation occurs as a result of the generation of electron–hole pairs. Initially, CP had a light-yellow colour. When analyzed using UV-vis spectroscopy, a distinct peak sharpened at 267 nm for CP and 249 nm for PR. The degradation percentage of CP, as determined from the spectrum in Fig. 5j, was 11%, 13%, 25%, 37%, 41%, 47%, 56%, and 67% at 15, 30, 45, 60, 75, 90, 105, and 120 minutes, respectively (see Fig. 5j). The ln plot *versus* time is represented in the corresponding Fig. 5(b & f). Approximately 67% of CP degraded into less harmful, simpler molecules, as illustrated in Fig. 5i. If there is no catalyst present in the reaction process, the degradation rate is much lesser, *i.e.*, 3%, as was observed with the help of UV-vis spectroscopy.

The chosen antibiotic, CP, is a pH-sensitive drug. The drug contains both acidic and basic forms due to the presence of primary functional groups; thus, CP shows a zwitter ionic form. The cationic state is concealed, when the pH is below 6.2, and it transitions to a zwitter ionic state between pH 6.2 and 9. An anionic state is acquired at pH values exceeding 9. The pHpzc (point zero charge) was determined using the drift method across a pH range, revealing a value of 6.6 for the NC. This suggests that the NC carries a positive charge, when the pH is below 6.6 and a negative charge when the pH exceeds 6.5. Considering that the adsorption was presumed to be more favourable towards the anionic form of CP, Fig. S7† illustrates the impact of pH on CP degradation. The catalytic degradation efficiency was observed to be highest at pH 7, which gradually diminished as the pH values shifted towards 9, 11, 5, and 3. In this context, the degradation efficiency was diminished in highly acidic or basic conditions due to the limited interaction

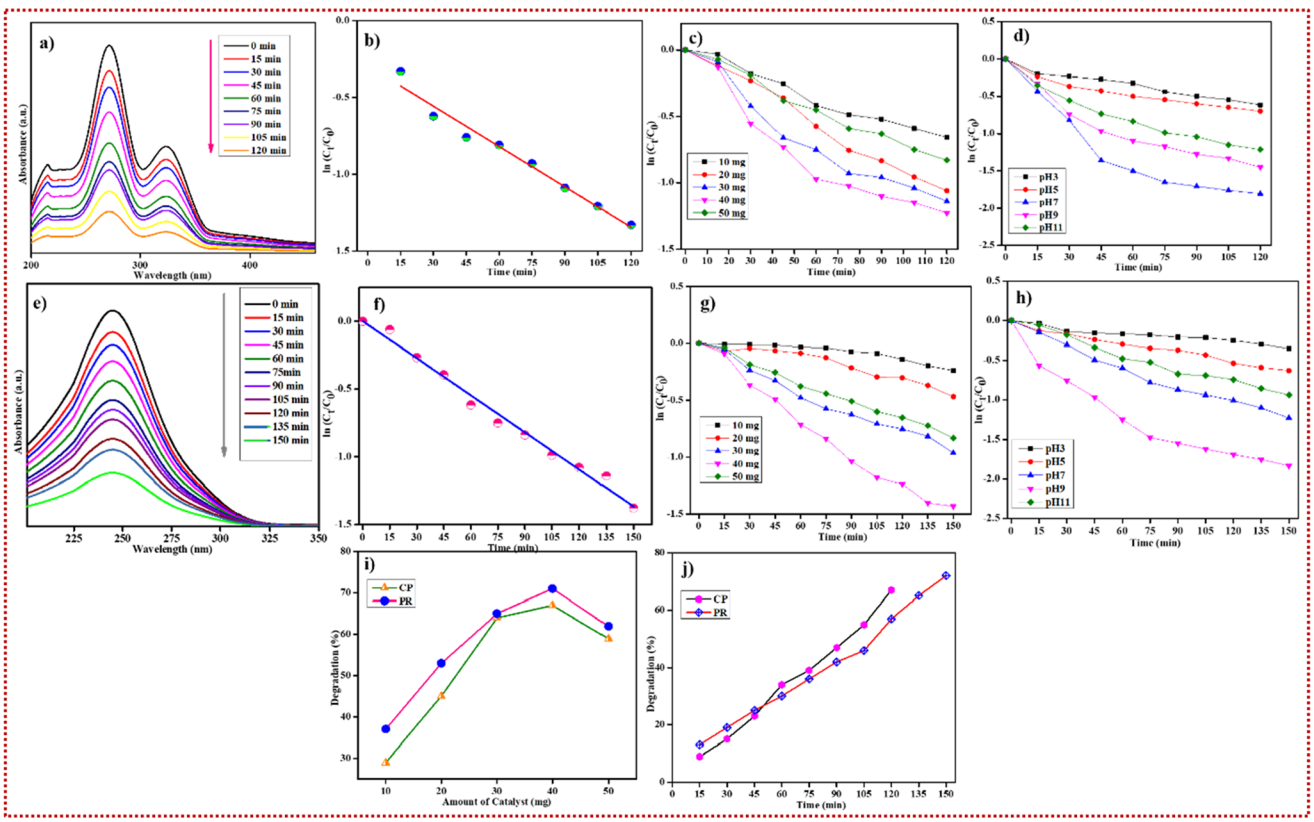

Fig. 5 Photo-degradation of pharma-waste using OSFTC. (a & e) CP and PR degradation, (b & f) show the ln plot for the reduction of CX and PM *vs.* time, (c & g) reveal the ln plot *vs.* time for different amount of catalytic dosage of CX and PM, (d & h) show the ln plot *vs.* the time for different pH variation toward CX & PM, (i) depicts the degradation percentage *vs.* the catalytic dosage for the completion of the reaction, & (j) reveals the degradation percentage *vs.* the time taken for the completion of the reaction.

of CP with the catalyst. Under such conditions, the presence of H^+ ions or OH^- ions primarily interacts with each other, rather than with the OSFTC. Similarly, the rate of degradation was analyzed for PR with the help of a UV-spectrophotometer. Under alkaline conditions, the degradation efficiency was hindered because of the inhibition of $^{\bullet}O_2^-$ radical formation. Across the pH range from 4 to 9 (as depicted in Fig. 5h), the catalyst exhibited effective degradation of PR. Conversely, under acidic conditions, the limited interaction between PR molecules and the OSFTC resulted in decreased efficiency of degradation. The effectiveness of catalytic degradation was highest at pH 9 (as shown in Fig. 5h), which gradually reduced when pH levels moved from 7 to 11, 5, and 3. Degradation percentages were observed at 13%, 19%, 25%, 31%, 36%, 42%, 46%, 57%, 65%, and 72% for 15, 30, 45, 60, 75, 90, 105, 120, 135, and 150 minutes, respectively. The ln plot was plotted against time which is shown in Fig. 5f. The parameters, such as the amount of catalyst, and the pH concentration were varied to test the optimal conditions for the degradation of the pharma-waste. With the help of Fig. 5(c & g), we can calculate how much amount of catalyst is exactly needed for the reaction to proceed with effective degradation of the noxious wastes. If we increase the catalytic dosage, the activity of the NC decreases because the adsorption of the pollutant to the OSFTC is lessened, decreasing the rate of degradation.

3.6 Hydrogenation of anthropogenic pollutant and reduction of Cr^{6+}

Forty millilitres of a common anthropogenic pollutant namely, 4-NPL (0.001 M), were taken in a beaker. Then 20 mg of the as-crafted OSFTC was added and it was stirred for 3 minutes for uniform distribution of the catalyst into the solution. Ten millilitres of 0.01 M $NaBH_4$ was added to it at a slow rate. The initial time was recorded as t_0, and the reaction response was examined periodically at regular time intervals (t) using UV-visible spectrophotometry. Initially, a distinct peak was observed at 320 nm for the nitrophenol solution. Upon the addition of $NaBH_4$, the peak from 320 nm shifted to 398 nm. This shift is known as a red shift as it occurs due to the conversion of 4-NPL to 4-nitrophenolate ion in the presence of $NaBH_4$. As time progressed, the peak at 398 nm decreased, while a new peak gradually emerged at 300 nm. This new peak corresponded to the 4-aminophenol (4-APL) and confirmed the kinetic conversion of 4-NPL to 4-APL. The degradation percentage of this conversion reaction was determined to be 92% within a duration of 27 minutes. Different reduction reactions were conducted by adjusting the dosage of the catalyst, and the analysis was performed using a UV-visible spectrophotometer. The results indicated that 20 mg of the catalyst (OSFTC) was sufficient for the conversion reaction of 4-NPL (0.001 M), as depicted in Fig. S21.† In the scenario of excess $NaBH_4$, the reaction exhibited pseudo-first-order kinetics, which was confirmed by a linear plot of $\ln(C_t/C_0)$ *versus* time. The spectrum thus obtained illustrated the kinetic transformation of 4-NPL to 4-APL, showcasing a linear correlation between $\ln(C_0/C_t)$ and time, which is indicative of pseudo-first-order kinetics. The equation governing the kinetics of the reaction was confirmed as follows:

$$dC_t/dt = -K_{np}C_t \quad (2)$$

$$\ln(C_t/C_0) = \ln(APL_t/APL_0) = -K_{np}t \quad (3)$$

The collective results for the OSFTC synthesized using the grinding method are outlined in Table 1. Similarly, the Cr^{6+} solution (40 mL; 2×10^{-3}) was taken in a separate beaker (Fig. 6). To this, 20 mg of OSFTC was added and 10 mL of 0.01 M $NaBH_4$. After the addition of the reducing agent, the initial time was noted as t_0, and the reaction mixture was tested at regular intervals of time (t). The reaction mixture was tested with the help of a UV-vis spectrophotometer. The intensity of the peak at 398 nm decreases and a new peak appears at 300 nm, confirming the decrease in the concentration of Cr^{6+} and the formation of Cr^{3+}. The reduction rate reaches 79% within 24 minutes. The reaction was tested only in the presence of a reducing agent, and the spectrum acquired after an hour implies that the reaction rate was not comparable to the reaction rate in the presence of the catalyst. If we consider sodium borohydride to be present in excess amounts, the reaction was validated to follow pseudo-first-order kinetics as shown in the plot of $\ln(C_0/C_t)$ *vs.* time, which presents a linear relationship. This plot shows the kinetics of the reduction reaction and signifies that the conversion followed pseudo-first-order kinetics.

3.7 Anti-bacterial inhibition of the bacterium

The NC synthesized in this study was evaluated for its antibacterial activity against both Gram-positive and Gram-negative bacteria using the colony-forming unit (CFU) method. Results indicate that the types of OSFTC effectively eradicate both Gram-positive and Gram-negative bacteria after exposure for up to 2 hours. Gram-positive bacteria (*e.g.*, *S. aureus*) and Gram-negative bacteria (*e.g.*, *E. coli*) were selected to assess the catalyst's efficacy. The polysaccharides associated with the cell membrane of *E. coli* interact to form a barrier that hinders nutrient intake by the cell. Similarly, bacteria like *S. aureus*, which lack a cell wall outside the bacterium, exhibit greater affinity toward the catalyst, leading to a higher inhibition rate. Mueller–Hinton agar medium was inoculated with diluted bacterial strains. The test samples were then applied to the culture medium. Subsequently, the inoculated plates were incubated at 37 °C for 24 hours. As a positive control for both kinds of bacteria, streptomycin was employed. Resazurin is a redox indicator that can be used in processes similar to those

Table 1 Table comparing the degradation efficiency of the OSFTC for all three pharma-wastes

	Photo-degradation (%)	
Name	CP	PR
OSFTC	67	71

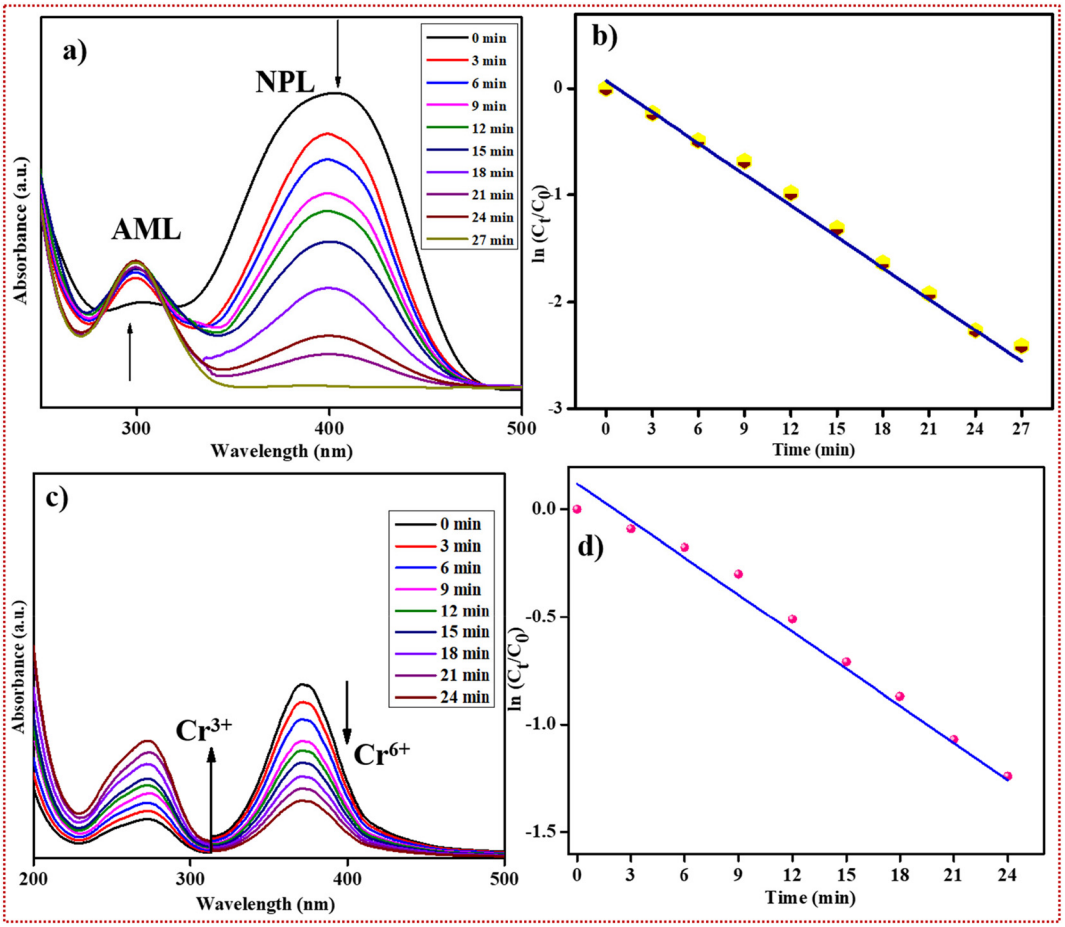

Fig. 6 (a) Reduction of 4-nitrophenol, (b) ln plot *vs.* time for 4-NPL reduction, (c) hexavalent chromium reduction, and (d) ln plot *vs.* time for chromium reduction.

that assess viable cell count using tetrazolium compounds because it is permeable to cells. Resazurin undergoes reduction to form a pink, fluorescent product called resorufin inside viable cells with active metabolism. By utilizing the resazurin, microbial growth can be detected in small solution volumes, such as in microliter plates, without the need for a spectrophotometer. After 24 hours, both cultures were monitored for growth using a UV-1800 spectrophotometer (Shimadzu, Japan) at a wavelength of 600 nm until it reached a final optical density (OD) of 1.0.

Two main theories exist regarding the mechanism by which NPs exert lethal effects on bacterial cells. According to the first theory, NPs interact directly with cellular components, including cell walls, cell membranes, and the cytoplasmic matrix, through electrostatic interactions. This interaction leads to membrane disruption, folding, and the formation of pores. The toxicity mechanisms of NPs vary based on factors, such as composition, surface modification, intrinsic properties, and the specific bacterial species involved. The antibacterial inhibition initiated by NPs is influenced primarily by two factors: (i) the physicochemical characteristics of the NPs and (ii) the type of bacteria targeted. This results in increased membrane permeability, deterioration of membrane integrity, bacterial cell death, and denaturation, degradation, and malfunction of cellular macromolecules, such as DNA, proteins, and enzymes. The second theory posits that NPs promote the generation of reactive oxygen species (ROS), leading to an increase in oxidative stress. This oxidative stress damages biomolecules and cell structures, ultimately resulting in bacterial cell death. The presence of metal NPs on the composite plays a vital role in ROS generation which in turn forms radicals that promote stress inside the cell. The stress caused during this process leads to bacterium cell death. There are four metal NPs present in the material as it has more electron density in it, creating a more facile pathway for ROS emergence. The relationship between exposure time and bacterial concentration is provided in the table, while the cell viability for both types of bacteria is illustrated in the accompanying Fig. 7(a–c). The mechanism of bacterial cell death is depicted in Fig. 7d. This is attributed to the higher metal content present in OSFTC, particularly Cu, which generates a larger amount of reactive oxygen species (ROS) compared to other metals. As a result, efficient eradication of bacteria is achieved. The oxidative stress induced by the generated reactive oxygen species

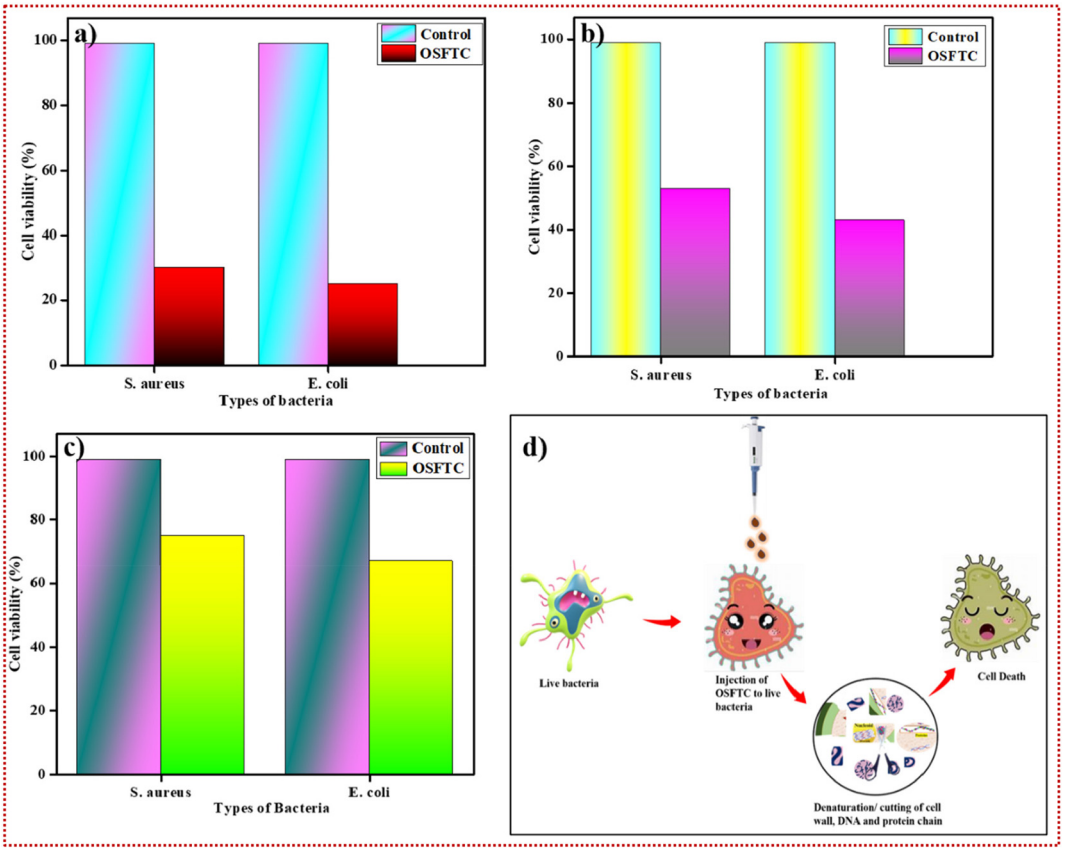

Fig. 7 (a–c) Cell viability percentage for 100 μL, 200 μL, and 300 μL of 20.3 × 10^{-2} M solution of OSFTC, (d) mechanism for killing bacterial cells *via* ROS species.

Table 2 MBC and MIC values for all the OSFTC toward both types of bacteria

	E. coli		*S. aureus*	
SAMPLE	MIC	MBC	MIC	MBC
OSFTC	42	51	85	129

(ROS) facilitates the killing action against bacteria. The minimum bactericidal concentration (MBC) and minimum inhibitory concentration (MIC) values were determined for both types of bacteria as shown in Table 2.

4. Discussion

4.1 The reason behind the action toward pharma-waste

(i) The rate of degradation of pharma-waste decreases for the as-crafted OSFTC. In general, the activity of the degradation rate increases when we utilize bimetallic instead of monometallic catalysts due to the synergism exhibited by both the NPs present on the material. Similarly, the trimetallic catalyst further increases the degradation rate than bimetallic materials. However, in the case of tetra-metallic composite, the activity of the catalyst shows a lesser degradation rate for the pharma-waste. This is because the electronic configuration of the four metals added imparts a paramagnetic behaviour. The paramagnetism exhibited by the four metals allows them to be attracted by the magnetic core, leading to the leaching-in of the metals added to the matrix formed by the magnetite NPs and the OSH powder. The leaching-in effect of metals leads to an increase in the magnetisation power as compared to the bare material. The leaching-in of metals in the OSFTC showed greater attraction toward the core of the nanohybrid composite, rather than the tendency to react with the pollutants. If the metal is attracted toward the core, the action of the metal NPs against the adsorbed pollutants lessens, and hence, the rate of degradation of pharma-waste diminishes.

(ii) Another reason is the polarization effect of the metal NPs, which takes place in accordance with Fajan's rule. Fajan's rule explains that as the size of an anion increases, its polarizability also increases. The ability of the anion to polarize depends on its size, and thus, the polarizing power is directly related to the size of the anion. Additionally, the electron density of the element plays a crucial role, enabling significant electron sharing and partial charge separation. The order of the polarising power is in the decreasing order of the 5d > 4d >

3d series. Since there is low polarising power among the 3d metals of the composite, the orientation of the 'd' orbitals in space lessens as compared to the 4d and 5d series. If the orientation is less, the interaction of the pollutants with the catalyst, and hence, the rate of degradation also decreases, even in the case of tetra-metallic NC.

5. Conclusion

In this work, the *Oryza sativa* husk is a versatile capping material for the preparation of a ternary composite because of the numerous amounts of hydroxyl groups present in it. This material combines with the magnetite particles to form a matrix-like material for the formation of the metal NPs. The successfully as-crafted NC was prepared *via* the manual solid-state method. The major advantage of this method is that it uses a null-solvent technique. The leaching-in of the metals toward the core of the nanohybrid increases the magnetic nature of the material. The as-crafted material was synthesized *via* several characterization analyses, such as XRD, FT-IR, FE-SEM, HR-TEM, VSM, XPS, and UV-vis analysis. This OSFTC material results in the degradation of pharma-waste, reduction of chromium hexavalent ion, and the hydrogenation of the anthropogenic pollutant. The rate of degradation is reduced as compared to the noble trimetallic or bimetallic NC as reported before. Furthermore, the OSFTC was tested for its recyclability, which was held for four cycles. The stability of the material was also good as confirmed with the help of XRD analysis. We improve the efficiency of the composite *via* doping of foreign material, leading to the most promising material for diverse applications.

Conflicts of interest

There are no conflicts to declare.

Acknowledgements

The authors acknowledge SRM Institute of Science and Technology for providing the major instrumentation facilities. The NRC-SRMIST and HRTEM Facility at SCIF were set up with support from MNRE (Project No. 31/03/2014-15/PVSE-R&D) by the Government of India.

References

1 K. B. Tan, M. Vakili, B. A. Horri, P. E. Poh, A. Z. Abdullah and B. Salamatinia, *Sep. Purif. Technol.*, 2015, **150**, 229–242.
2 B. A. Aragaw and A. Dagnaw, *Ethiop. J. Sci. Technol.*, 1970, **12**, 125–137.
3 R. H. Gadah and A. S. Basaleh, *Ceram. Int.*, 2020, **46**, 1690–1696.
4 R. Kaur, D. Singh, A. Kumari, G. Sharma, S. Rajput, S. Arora and R. Kaur, *Int. J. Environ. Sci. Technol.*, 2023, **20**, 3537–3560.
5 J. Kaushal, M. Khatri and S. K. Arya, *Ecotoxicol. Environ. Saf.*, 2021, **207**, 111483.
6 L. E. Shi, Z. H. Li, W. Zheng, Y. F. Zhao, Y. F. Jin and Z. X. Tang, *Food Addit. Contam.: Part A*, 2014, **31**, 173–186.
7 U. Bogdanović, V. Lazić, V. Vodnik, M. Budimir, Z. Marković and S. Dimitrijević, *Mater. Lett.*, 2014, **128**, 75–78.
8 N. Liu, N. Lu, Y. Su, P. Wang and X. Quan, *Sep. Purif. Technol.*, 2019, **211**, 782–789.
9 S. Marimuthu, A. J. Antonisamy, S. Malayandi, K. Rajendran, P. C. Tsai, A. Pugazhendhi and V. K. Ponnusamy, *J. Photochem. Photobiol., B*, 2020, **205**, 111823.
10 Z. I. Ali, O. A. Ghazy, G. Meligi, H. H. Saleh and M. Bekhit, *J. Inorg. Organomet. Polym. Mater.*, 2018, **28**, 1195–1205.
11 A. V. Rane, K. Kanny, V. K. Abitha and S. Thomas, in *Synthesis of Inorganic Nanomaterials: Advances and Key Technologies*, Elsevier, 2018, pp. 121–139.
12 Y. Xiong, L. Huang, S. Mahmud, F. Yang and H. Liu, *Chin. J. Chem. Eng.*, 2020, **28**, 1334–1343.
13 N. Raghavan, S. Thangavel and G. Venugopal, *Mater. Sci. Semicond. Process.*, 2015, **30**, 321–329.
14 D. Majumdar, *ChemElectroChem*, 2021, **8**, 291–336.
15 R. Stephanie, M. W. Kim, S. H. Kim, J. K. Kim, C. Y. Park and T. J. Park, *TrAC, Trends Anal. Chem.*, 2021, **135**, 116159.
16 M. Hasanzadeh, A. Simchi and S. H. Far, *J. Ind. Eng. Chem.*, 2020, **81**, 405–414.
17 H. Pezeshki, M. Hashemi and S. Rajabi, *Heliyon*, 2023, **9**, e14246.
18 H. K. Patel, R. K. Kalaria, P. H. Jokhakar, C. R. Patel and B. Y. Patel, in *Development in wastewater treatment research and processes*, Elsevier, 2022, pp. 385–400.
19 A. V. Munde, B. B. Mulik, P. P. Chavan and B. R. Sathe, *Electrochim. Acta*, 2020, **349**, 136386.
20 R. Ravichandran, K. Annamalai, A. Annamalai and S. Elumalai, *Colloids Surf., A*, 2023, **664**, 131117.
21 A. Ahmad, A. S. Qureshi, L. Li, J. Bao, X. Jia, Y. Xu and X. Guo, *Colloids Surf., B*, 2016, **143**, 490–498.
22 G. Pal, P. Rai and A. Pandey, *in Green Synthesis*, Characterization and Applications of Nanoparticles, Elsevier, 2018, pp. 1–26.
23 A. Gour and N. K. Jain, *Artif. Cells, Nanomed., Biotechnol.*, 2019, **47**, 844–851.
24 W. Yuan, Z. Lu and C. M. Li, *J. Mater. Chem. A*, 2013, **1**, 6416–6424.
25 W. Yuan, J. Fu, K. Su and J. Ji, *Colloids Surf., B*, 2010, **76**, 549–555.
26 M. S. Usman, M. E. El Zowalaty, K. Shameli, N. Zainuddin, M. Salama and N. A. Ibrahim, *Int. J. Nanomed.*, 2013, **8**, 4467–4479.

27 J. P. Ruparelia, A. K. Chatterjee, S. P. Duttagupta and S. Mukherji, *Acta Biomater.*, 2008, **4**, 707–716.
28 P. N. Babaso and H. Sharanagouda, *Int. J. Curr. Microbiol. Appl. Sci.*, 2017, **6**, 1144–1156.
29 H. Houcini, F. Laghrib, M. Bakasse, S. Lahrich and M. A. El Mhammedi, *Int. J. Environ. Anal. Chem.*, 2020, **100**, 1566–1577.
30 M. Alle, S. H. Lee and J. C. Kim, *J. Mater. Sci. Technol.*, 2020, **41**, 168–177.
31 K. Ma, A. Sinha, X. Dang and H. Zhao, *J. Electrochem. Soc.*, 2019, **166**, B147–B154.
32 R. S. Jones, R. R. Draheim and M. Roldo, *Appl. Sci.*, 2018, **8**, 673.
33 J. Talapko, T. Matijević, M. Juzbašić, A. Antolović-Požgain and I. Škrlec, *Microorganisms*, 2020, **8**, 1–13.
34 A. S. Hassanien and U. T. Khatoon, *Phys. B: Condens. Matter*, 2019, **554**, 21–30.
35 T. M. Hakami, A. M. Davarpanah, A. Rahdar and S. D. Barrett, *J. Mol. Struct.*, 2018, **1165**, 344–348.
36 L. Li, R. Niu and Y. Zhang, *RSC Adv.*, 2018, **8**, 12428–12438.
37 S. Liu, B. Yu, S. Wang, Y. Shen and H. Cong, *Adv. Colloid Interface Sci.*, 2020, **281**, 102165.
38 J. Shan, L. Wang, H. Yu, J. Ji, W. A. Amer, Y. Chen, G. Jing, H. Khalid, M. Akram and N. M. Abbasi, *Mater. Sci. Technol.*, 2016, **32**, 602–614.
39 J. Liu, S. Z. Qiao, Q. H. Hu and G. Q. Lu, *Small*, 2011, **7**, 425–443.
40 K. Annamalai, A. Annamalai, R. Ravichandran, S. Elumalai, S. Rajendran and N. Tsapis, Waste Management Recyclable e-waste Derived Carbon Dots (e-CDs) for Detection of Two-fold Metal ions and Degradation of BTB Dye Powered by Editorial Manager® and ProduXion Manager® from Aries Systems Corporation.
41 C. Prasad, H. Tang and I. Bahadur, *J. Mol. Liq.*, 2019, **281**, 634–654.
42 A. M. Abdel-Wahab, A. S. Al-Shirbini, O. Mohamed and O. Nasr, *J. Photochem. Photobiol., A*, 2017, **347**, 186–198.
43 T. Ahamad, M. Naushad and S. M. Alshehri, *Chem. Eng. J.*, 2021, **417**, 127969.
44 L. Yang, L. E. Yu and M. B. Ray, *Environ. Sci. Technol.*, 2009, **43**, 460–465.
45 S. S. Imam, R. Adnan and N. H. Mohd Kaus, *Toxicol. Environ. Chem.*, 2018, **100**, 518–539.
46 N. Jallouli, K. Elghniji, H. Trabelsi and M. Ksibi, *Arabian J. Chem.*, 2017, **10**, S3640–S3645.
47 Z. Jiang, J. Xie, D. Jiang, X. Wei and M. Chen, *CrystEngComm*, 2013, **15**, 560–569.
48 Q. Cai, C. Liu, C. Yin, W. Huang, L. Cui, H. Shi, X. Fang, L. Zhang, S. Kang and Y. Wang, *ACS Sustainable Chem. Eng.*, 2017, **5**, 3938–3944.
49 A. Annamalai, K. Annamalai, R. Ravichandran, S. Bharathkumar and S. Elumalai, *Colloids Surf., A*, 2022, **652**, 129800.